Earth and Planetary Science Letters 536 (2020) 116161

Contents lists available at ScienceDirect

Earth and Planetary Science Letters

www.elsevier.com/locate/epsl

Thermal conductivity near the bottom of the Earth's lower mantle: Measurements of pyrolite up to 120 GPa and 2500 K

Zachary M. Geballe [a,*], Nathan Sime [b], James Badro [c], Peter E. van Keken [b], Alexander F. Goncharov [a]

[a] Geophysical Laboratory, Carnegie Institution for Science, Washington DC, USA
[b] Department of Terrestrial Magnetism, Carnegie Institution for Science, Washington DC, USA
[c] Institut de Physique du Globe de Paris, Université de Paris, 75005 Paris, France

ARTICLE INFO

Article history:
Received 17 November 2019
Received in revised form 6 February 2020
Accepted 13 February 2020
Available online xxxx
Editor: J. Brodholt

Keywords:
Earth's heat loss
diamond anvil cell
finite element methods

ABSTRACT

Knowledge of thermal conductivity of mantle minerals is crucial for understanding heat transport from the Earth's core to mantle. At the pressure-temperature conditions of the Earth's core-mantle boundary, calculations of lattice thermal conductivity based on atomistic models have determined values ranging from 1 to 14 W/m/K for bridgmanite and bridgmanite-rich mineral assemblages. Previous studies have been performed at room temperature up to the pressures of the core-mantle boundary, but correcting these to geotherm temperatures may introduce large errors. Here we present the first measurements of lattice thermal conductivity of mantle minerals up to pressures and temperatures near the base of the mantle, 120 GPa and 2500 K. We use a combination of continuous and pulsed laser heating in a diamond anvil cell to measure the lattice thermal conductivity of pyrolite, the assemblage of minerals expected to make up the lower mantle. We find a value of $3.9^{+1.4}_{-1.1}$ W/m/K at 80 GPa and 2000 to 2500 K and $5.9^{+4.0}_{-2.3}$ W/m/K at 124 GPa and 2000 to 3000 K. These values rule out the highest calculations of thermal conductivity of the Earth's mid-lower mantle (i.e. $k < 6$ W/m/K at 80 GPa), and are consistent with both the high and low calculations of thermal conductivity near the base of the lower mantle.

1. Introduction

It is estimated that up to 16 TW of heat flows from the Earth's core into the overlying mantle (Pozzo et al., 2012). Heat transfer across the base of the mantle is the rate limiting step of how much heat is extracted from the core and thereby controls the dynamics of the Earth's core, the generation of its magnetic field, and the energy budget of mantle convection. One key factor that influences the magnitude of core-mantle boundary (CMB) heat flux is the thermal conductivity of the assemblage of minerals that makes up the lowermost mantle, which can be approximated as 75% bridgmanite, 19% ferropericlase and 6% $CaSiO_3$ perovskite (Stackhouse et al., 2015). Determining the thermal conductivity of these minerals at the high pressure and temperature is therefore a crucial step in understanding the core-mantle heat flux and its many ramifications on dynamics of the deep Earth.

The lattice thermal conductivity of bridgmanite has been calculated using a variety of classical- and quantum-mechanics based methods, providing a key starting point for calculation of pyrolite's thermal conductivity. The discrepancies between results from different research groups are large. At 120 GPa and 2500 K, for example, five recent studies calculate thermal conductivity of $MgSiO_3$ bridgmanite to be 1, 5, 6.5, 9.5, and 14 W/m/K (Tang et al., 2014; Dekura et al., 2013; Stackhouse et al., 2015; Ammann et al., 2014; Haigis et al., 2012). A sixth study extrapolates to 8.3 W/m/K upon scaling from 300 K to 2500 K (Ghaderi et al., 2017).

The discrepancies reduce somewhat when estimating total conductivity for pyrolite by adding bridgmanite's radiative thermal conductivity and averaging with conductivities of ferropericlase and calcium perovskite. For example, Tang et al. (2014) estimates 3.5 W/m/K total conductivity whereas Stackhouse et al. (2015) estimates 10 W/m/K at 125 GPa and 2500 K.

Laboratory measurements of lattice thermal conductivity of mantle minerals have been conducted up to the pressure of the core-mantle boundary, but measurements at pressure above 40 GPa have always been at (or near) room temperature (300 to 500 K). Two different research groups measured conductivity of bridgmanite to be 15 to 25 W/m/K at 120 GPa and room

* Corresponding author.
E-mail addresses: zgeballe@carnegiescience.edu (Z.M. Geballe), nsime@carnegiescience.edu (N. Sime), badro@ipgp.fr (J. Badro), pvankeken@carnegiescience.edu (P.E. van Keken), agoncharov@carnegiescience.edu (A.F. Goncharov).

https://doi.org/10.1016/j.epsl.2020.116161
0012-821X/

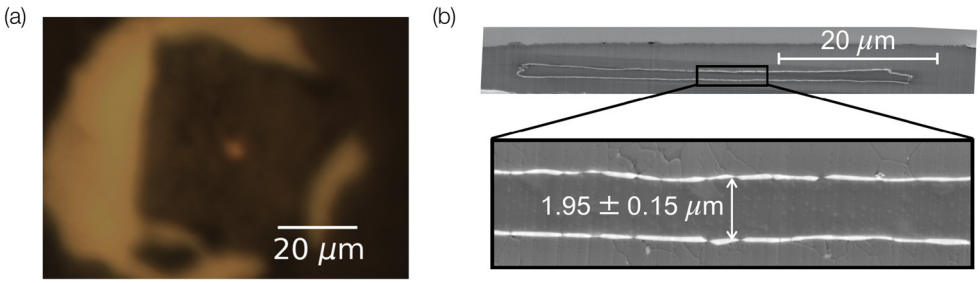

Fig. 1. (a) Iridium-coated pyrolite sample heated at 80 GPa. The hot spot is the white spot in the middle. The sample is illuminated from the back and front by white light. (b) Secondary electron image of cross section of the iridium-coated pyrolite sample surrounded with KCl, recovered from 80 GPa, covered in a tungsten protection layer (light grey) and sliced in half by a focused ion beam.

temperature, with conductivity decreasing with increasing Fe or Al substitution (Ohta et al., 2012; Okuda et al., 2017; Hsieh et al., 2017). One high-temperature study of thermal conductivity of bridgmanite reached the pressure of the uppermost lower mantle, and measured 8 W/m/K at 1070 K for pure $MgSiO_3$ and 4 W/m/K for $Mg_{0.97}Fe_{0.03}SiO_3$ (Manthilake et al., 2011). Laboratory measurements have also been made on lattice thermal conductivity of ferropericlase to CMB pressures at room temperature (Dalton et al., 2013; Imada et al., 2014; Goncharov et al., 2015; Hsieh et al., 2018), of MgO to 32 GPa and 2500 K (Goncharov et al., 2009), and of the pressure derivative of MgO up to 40 GPa and 2000 K (Rainey and Kavner, 2014). Radiative thermal conductivity has been experimentally shown to be relatively small (< 1 W/m/K) even at high temperatures (Lobanov et al., 2017, 2019a,b).

Overall, published experimental determinations of lattice thermal conductivity provide a starting point for estimating thermal conductivity at the base of the Earth's mantle, but large extrapolation is required to reach the appropriate conditions of pressure and temperature.

To date, no laboratory measurements have been reported for thermal conductivity of bridgmanite, ferropericlase, or Ca-perovskite at pressures and temperatures simultaneously above 40 GPa and 500 K. The reason is the extreme challenge of maintaining a stable high temperature state while quickly heating part of the sample and measuring the time-dependent response as heat flows through the sample.

Here we present the first measurements of thermal conductivity of pyrolite at several pressures and temperatures along the Earth's geotherm from 40 to 124 GPa at 1900 to 2900 K. These measurements combine several cutting-edge techniques: pulsed and continuous laser-heating, time-resolved temperature measurements, double-sided iridium coating of thin samples, and finite element modeling of heat flow in a diamond anvil cell.

2. Methods

2.1. Experimental methods

We present the results of five high pressure runs in laser-heated diamond anvil cells. In each run, an iridium-coated pyrolite sample is compressed, laser heated to ~2000 K, and pulsed laser heated from one side. Thermal emissions are collected as a function of time and space, and are analyzed to determine thermal conductivity of the pyrolite sample.

Each diamond cell is loaded with a ~6 μm-thick slab of pyrolite glass coated with 2 nm of titanium and 43 ± 5 or 178 ± 5 nm of iridium, surrounded by potassium-chloride or argon, and pressed inside the hole of a rhenium gasket. The titanium serves as an adhesion layer to prevent the iridium from delaminating prior to the high pressure run. The first set of experiments used the thinner iridium coating, which may have contributed to failure of several experiments not reported here, in which holes formed in the iridium layer upon pulsed heating. The thicker coating was used for the second set of experiments. The potassium-chloride or argon serves as the pressure medium and thermal insulation from the diamonds. In the case of argon, the iridum-pyrolite-iridium sandwich was placed atop three ruby spheres before gas-loading in order to separate it from one diamond. The pyrolite glass is the same one used in previous measurements of radiative conductivity (Lobanov et al., 2019a). It was synthesized by grinding together $CaCO_3$, MgO, Al_2O_3, SiO_2 and Fe_2O_3, decarbonating at 850 °C and fusing in a laser levitation furnace at 2000 °C in a gas with oxygen fugacity 0.7 log units above the iron-wüstite buffer; see Lobanov et al. (2019a) for details. The glass's chemical composition was measured by Lobanov et al. (2019a) to be 38.15 ± 0.12 wt% MgO, 46.6 ± 0.1 wt% SiO_2, 2.16 ± 0.03 wt% CaO, 8.66 ± 0.12 wt% FeO, and 4.24 ± 0.06 wt% Al_2O_3.

The subsequent compression and heating procedure is similar to that presented in McWilliams et al. (2015) and Konôpková et al. (2016). Samples are compressed to the desired pressure, heated to ~2500 K to convert the glass starting material to a polycrystalline assemblage of minerals (bridgmanite, ferropericlase, calcium-perovskite), and pulsed-heated from one side while measuring time-resolved thermal emissions on a streak camera and spatially-resolved thermal emissions on a CCD camera. Several sets of thermal emissions data are collected from each side to make sure temperatures do not drift substantially through time. This also ensures that there is no residual amorphous material near the hotspot that continues to crystallize during the experiment. The samples are decompressed to ambient pressure, cross sections are cut with a focused ion beam, thickness is measured, and chemical composition is mapped in a SEM. Fig. 1 shows an example of a compressed sample and its cross section after decompression. Further details are presented in the Supplementary Material.

2.2. Data analysis

We divide the analysis into data reduction, finite element modeling, and error analysis. In the first step, the raw data is reduced to determine temperature as a function time and location on the two iridium surfaces. Then a finite element model is used to find best-fit values of thermal conductivity of the pyrolite sample, k_{pyro}, and the insulating medium, k_{ins}, while fixing all other parameters to their estimated values. Finally, all parameters are co-varied with k_{pyro} and k_{Ir} is co-varied with both k_{pyro} and k_{ins} to determine the uncertainty in pyrolite's thermal conductivity, $\sigma_{k_{\text{pyro}}}$.

2.2.1. Data reduction

Each image from the streak camera is reduced to normalized temperature as a function of time in a five step process. First, measured intensity is corrected for geometrical distortion in the streak tube. Second, it is corrected for bias in the conversion efficiency from emitted photon to measured intensity. The bias is both in

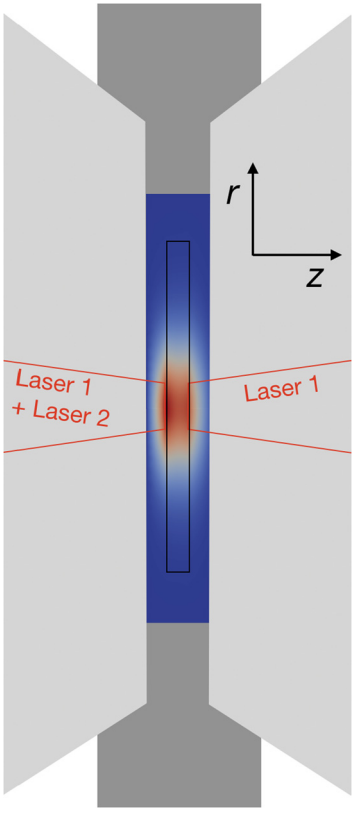

Fig. 2. Experimental setup for thermal conductivity measurements. An iridium-coated slab of pyrolite (black outline) is heated from both sides by a continuous laser (Laser 1) and from the "pulsed side" by a pulsed laser (Laser 2). Thermal insulation separates the sample from the diamond culets (light grey) and gasket (dark grey). Blue to red shading represent simulated temperatures of pyrolite, iridium, and insulation from 300 K (blue) to 2500 K (red). (For interpretation of the colors in the figure(s), the reader is referred to the web version of this article.)

time and wavelength, and is corrected with a reference image from a tungsten lamp heated to a known temperature. Third, the Planck function is fit to intensity averaged over a relatively wide time-window (3 or 10 μs) using both temperature and emissivity as fitting parameters. Fourth, emissivity is fixed to the value from the third step and the Planck function is fit to the intensity averaged over a set of narrow time-slices. For example, Planck fits to forty slices of 0.5 μs width generate the ~20 μs-duration temperature-time curves in Fig. S4. The fifth step is reduction to a normalized temperature, which enables efficient comparison of measurements to each other and to finite element models. This normalization has no effect on the model parameters needed to match the data, besides the parameter describing the magnitude of laser power.

In addition to measuring the temporal evolution of temperature, the spatial distribution of thermal emissions from the CCD image are reduced to temperature versus distance. Briefly, we reference the peak intensity on the CCD camera to the temperature measured on the streak camera prior to heating pulses. We then use the Planck function to determine $T(x)$. This analysis gives us the width of the hotspot, T_{FWHM}, which is an important input for the finite element model used to infer thermal conductivity. Here, 'FWHM' means the full width at half the maximum temperature above the 300 K baseline temperature. Details are described in the Supplementary Material.

2.2.2. Finite element modeling

Computational modeling is required to determine the thermal conductivity of our samples, because we lack an analytical model to the three-dimensional heat flow of this experiment. We solve the governing heat equation using finite element modeling based on the FEniCS project (Alnæs et al., 2015). We model the diamond anvil assembly with an axisymmetric geometry with rotational symmetry around the center of the assembly. We assume 300 K Dirichlet boundary conditions at $r = 100$ μm and $z = \pm 40$ μm, where r is radius from the center and z is the axial distance from the center of the sample (Fig. 2). Thicknesses of sample and insulation match those measured in each experiment. As in Hsieh et al. (2017), we assume the volume of the iridium coating varies with pressure according to its equation of state and that its surface area matches that of the sample. In other words, the iridium adheres perfectly to the sample as the sample flattens under pressure. This means the iridium thins by 5 to 10% less than the sample due to the fact that iridium is less compressible than pyrolite. All thicknesses are listed in Table 1. An example of the finite element mesh is shown in Fig. S6.

The free parameters in this model are thermal conductivities of pyrolite, iridium and the insulator (KCl or Ar). To restrict the parameter space that must be explored, we assume the lower bound $k_{\mathrm{Ir}} > 30$ W/m/K (see Supplement for details). All other model parameters are either measured in this study (such as the parameters describing the geometry), measured in other studies (density), assumed (heat capacity), or are considered to negligibly affect the modeled temperature evolution of the iridium surfaces (such as the thermal conductivity of the gasket and diamond, and the distance to boundaries of the modeled domain). The < 2 nm thick titanium adhesion layer is not modeled, since it is much thinner than the iridium layer and has similar conductive properties, meaning it provides negligible resistance to axial heat flow, negligible heat capacity, and negligible radial conductance.

In reality, all three free parameters, k_{pyro}, k_{Ir}, and k_{ins}, depend on temperature, but we do not model their temperature-dependencies here. Instead, our main results are the values of k_{pyro} that are consistent with our data at each pressure, P, and range of temperatures, $T \pm \sigma_T$; see Fig. 4b and Table 2 for values of P, T, σ_T, and estimated pressure uncertainty, σ_P.

We model the background and pulsed heating with two different methods in our determination of k_{pyro} and its uncertainty. Both methods solve the heat equation on the same domain, but they differ in one important way. 'Method Q' includes a heating term Q on the pulsed-side iridium surface, $Q(r,t) = Q_0(r)(1 + dQ(t))$, where t is time, Q_0 is a background term, and dQ is the time-dependent heating pulse. In 'method T' we impose a time-dependent Dirichlet boundary condition at the pulsed-side iridium surface, $T(r,t) = 300 + T_0(r)(1 + dT(t))$, where T is absolute temperature in K, T_0 is a background term, and dT describes the effect of the pulse heating. Method Q models the thermal evolution that is closer to the reality we expect: the spatial distribution of absorbed laser power remains constant throughout the heating pulse. Method T models the case of a constant spatial distribution of temperature, but in reality we expect a slight widening of the temperature distribution throughout the duration of the pulse. The two methods result in best fit values of k_{pyro} within 5% of each other for four of our six data points, and up to 25% for the data points at 40 and 68 GPa. The comparison of results obtained with these two methods is provided in Table S1 and the implementation of the methodologies is further described in the Supplementary Information.

We use the two methods in the following sequence. First, we use method T to fit measurements of temperature vs. time and temperature vs. distance. In this step we assume the values of k_{Ir} listed in Table 1 and fit for k_{pyro} and k_{ins}. Second, we remove the assumption of k_{Ir} and search for all values of (k_{pyro}, k_{Ir}, k_{ins}) that fit the data. From this search, along with uncertainty propagation from all other parameters (as describe in the Supplementary Material), we determine the uncertainty $\sigma^T_{k_{\mathrm{pyro}}}$. Third, we use these

Table 1
Key inputs to the finite element model used to infer thermal conductivity of pyrolite. Iridium thermal conductivity is used as a starting guess and is an assumption for the best fit, k_{pyro}, but not for uncertainty analysis. Insulator refractive index, n_{ins}, at room temperature is used to determine thicknesses of insulation on each side of the sample, $d_{\mathrm{ins,pside}}$ and $d_{\mathrm{ins,oside}}$, assuming the values from Goncharov (unpublished) for KCl and Chen et al. (2010) for Ar.

Run	P (GPa)	ρ (kg/m^3) pyrolite	Ir	insulator	c_v (J/K/kg) pyrolite	Ir	insulator	k (W/m/K) Ir	T_{FWHM} (μm)	d_{pyro} (μm)	d_{Ir} (μm)	$d_{\mathrm{ins,pside}}$ (μm)	$d_{\mathrm{ins,oside}}$ (μm)	ins. material	n_{ins}
1	40	4676	24781	4556	1158	130	623	278	9.5	2.47	0.098	7.7	6	Ar	1.9
2	41	4689	24822	3488	1158	130	668	280	12	2.85	0.025	9.9	8.8	KCl	1.9
3	62	4944	25767	3860	1158	130	668	318	10	2.5	0.078	3.2	6.4	KCl	2
4	68	5019	27136	3957	1158	130	668	330	18	1.4	0.019	5.7	5.8	KCl	2
4	80	5164	26504	4131	1158	130	668	352	13.2	1.84	0.062	3.2	6.3	KCl	2.05
5	124	5573	27136	4671	1158	130	668	433	8.5	1.7	0.039	1.6	2.1	KCl	2.16

results as a starting point to find the best-fit of the conductivity k^{Q}_{pyro} with method Q. Examples of best-fit models of method Q to data from 80 GPa data is shown in Fig. 3. Finally, we assume the uncertainty in results obtained with method Q is proportional to that determined in method T, that is $\sigma^{Q}_{k_{\mathrm{pyro}}} = \sigma^{T}_{k_{\mathrm{pyro}}} k^{Q}_{\mathrm{pyro}} / k^{T}_{\mathrm{pyro}}$. We avoid searching the parameter space to determine $\sigma^{Q}_{k_{\mathrm{pyro}}}$ explicitly, because the computational effort needed for method Q is significantly larger than that for method T for reasons described in the Supplementary Material. The final results k^{Q}_{pyro} and $\sigma^{Q}_{k_{\mathrm{pyro}}}$ are reported without the superscript "Q" in all summary figures and Table 2.

Uncertainty in $\sigma^{T}_{k_{\mathrm{pyro}}}$ is determined by quadrature addition of uncertainties from: (i) the range of values of k_{pyro} that fit the data when exploring the three-dimensional parameter space $\mathbf{k} = (k_{\mathrm{pyro}}, k_{\mathrm{ins}}, k_{\mathrm{Ir}})$; and (ii) uncertainty propagated from uncertainty in seven measured or theoretically estimated parameters. These seven parameters are pyrolite thickness, iridium thickness, other-side insulator thickness, FWHM of spatial distribution of temperature, and ρc_v of pyrolite, iridium, and the insulator. All other model parameters have minimal effect on the best-fit value of k_{pyro}. Table S1 lists all uncertainties.

3. Results and discussion

The newly determined thermal conductivity of pyrolite is between 3 and 10 W/m/K at all pressures from 40 to 124 GPa (Fig. 4). This is consistent with both the low and high calculations of thermal conductivity of pyrolite near the base of the lower mantle, but does not permit any estimates lower than those of Tang et al. (2014) or higher than those of Stackhouse et al. (2015). At shallower depths, near the middle of the lower mantle, our most precise datum rules out the conductivity calculations with $k_{\mathrm{pyro}} > 6$ W/m/K (Stackhouse et al., 2015). At even lower pressures, our 40 GPa data rule out the conductivity calculations with $k_{\mathrm{pyro}} < 3.5$ W/m/K (Tang et al., 2014).

While our data are consistent with previous laboratory measurements of bridgmanite at lower pressure and/or temperature, comparisons are complicated by differences in sample composition (Fig. 5). The conductivity of Fe-bearing bridgmanite at 26 GPa and 1000 K was measured by Manthilake et al. (2011) to be 4 W/m/K, which matches our measurements of pyrolite at 40 and 41 GPa within the error bars. Indeed, we expect little change overall since the higher temperatures studied here reduce the conductivity of Fe-bearing bridgmanite by a few tens of percent, and the addition of magnesiowüstite likely increases it by a few tens of percent. Compared to the room temperature experimental data of Fe-bearing bridgmanite (Hsieh et al., 2017), the approximately two-fold lower thermal conductivity measured here suggests that the effect of heating from 300 to 2500 K, which likely decreases k, outweighs the addition of ferropericlase, which likely increases k.

Our results suggest that the pressure dependence of thermal conductivity is relatively small, and that it could be either positive or negative. Assuming a linear dependence on pressure over the range 40 to 124 GPa, the slope dk_{pyro}/dP is estimated to be between -0.04 and +0.04 W/m/K/GPa. Even the greatest values in this range are less than slopes for the theoretically-determined conductivities of pyrolite in Stackhouse et al. (2015) ($dk/dP = 0.06$) and for bridgmanite in four other studies (Dekura et al., 2013; Haigis et al., 2012; Ghaderi et al., 2017; Ammann et al., 2014), but in agreement with the pressure-derivative calculated for bridgmanite in Tang et al. (2014). In all cases, we are comparing values of dk/dP along the 2500 K isotherm. The relatively small slope measured here is broadly consistent with the room-temperature measurements of Fe-bearing bridgmanite of Hsieh et al. (2017), which show $dk_{\mathrm{pyro}}/dP \sim 0.03$ W/m/K/GPa at pressures above 40

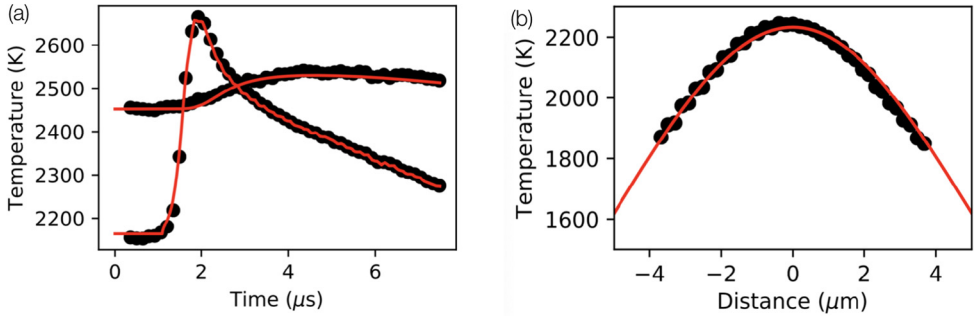

Fig. 3. Example of measurements and fits at 80 GPa. (a) Temperature vs. time on pulsed-heated side (2100 to 2700 K curve) and other side (2450 to 2550 K curve). (b) Temperature vs. distance from center of hotspot on pulsed-heated side at the time corresponding to 0 μs in (a).

Table 2
Results of finite element analysis. Best fits, k_{pyro} and k_{ins}, assume listed values of k_{Ir}. Uncertainties, σ_k, and upper-bounds, k^{max}, do not assume any particular value of k_{Ir}.

				Pyrolite				Insulator			Iridium	
P	σ_P	T	σ_T	k_{pyro}	σ_k^-	σ_k^+	D_{pyro}	k_{ins}	$k_{\text{ins}}^{\text{max}}$	ins.	k_{Ir}	$k_{\text{Ir}}^{\text{max}}$
(GPa)		(K)		(W/m/K)			(mm^2/s)	(W/m/K)		material	(W/m/K)	
40	4	2290	320	5	-1.4	+1.9	0.92	2	5.7	Ar	278	600
41	4.1	2180	160	6.1	-2.3	+2.9	1.12	3	8.9	KCl	280	1600
62	6.2	2200	200	4.6	-1.8	+3	0.8	12.6	20.1	KCl	318	1300
68	6.8	2050	150	4.3	-1.4	+2.3	0.74	4.1	6.6	KCl	330	1400
80	8	2280	210	3.9	-1.1	+1.4	0.65	10	18.2	KCl	352	1300
124	12.4	2460	380	5.9	-2.3	+4	0.91	10.1	12.5	KCl	433	2000

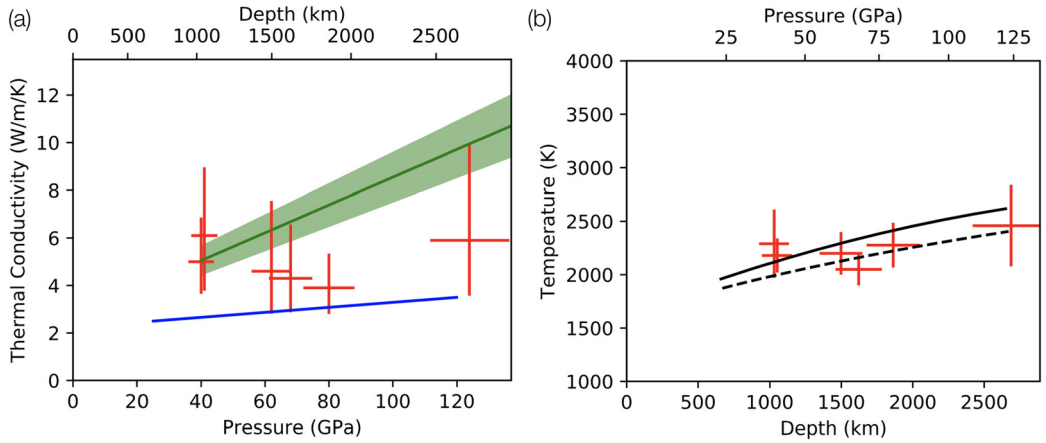

Fig. 4. (a) Thermal conductivity of pyrolite at 1900 to 2900 K. Experimental data from this study (red symbols). Theoretical calculations from Stackhouse et al. (2015) (interpolated to 2500 K; green) and from Tang et al. (2014) (extrapolated to their estimated geotherm ranging from 2000 to 2500 K; blue). (b) Temperature of data points presented here (red) as a function of depth along with the estimated lower mantle geotherms of Katsura et al. (2010) (solid black) and Brown and Shankland (1981) (dashed black).

GPa. More detailed analysis of pressure trends awaits further data. The possible influence of the spin-transition is especially intriguing, as suggested by Hsieh et al. (2017).

Our highest pressure data point at 124 GPa and 2100 to 2800 K constrains the thermal conductivity near the base of the mantle to the range 3–10 W/m/K. The lower end of this range overlaps with the theory-based estimate of Tang et al. (2014), while the upper limit of this range is slightly lower than the lowest estimate of Stackhouse et al. (2015).

The thermal conductivity of the lowermost mantle is one piece of a complicated puzzle that needs to be solved to better understand the dynamics of the Earth's mantle and core-mantle interaction. The cooling of the core is largely dominated by the ability of the lower mantle to absorb the heat flowing from the core, which in turn is controlled by the thermal conductivity, temperature gradients, and speed of convective flow of the lowermost mantle. The speed of convective flow is determined by rheology combined with thermal and chemical buoyancy forces. Our current understanding of lower mantle rheology is mostly incomplete except for possible inferences of the broad viscosity structure from geodetic and geodynamic observations (e.g., Mitrovica and Forte, 1997; Rudolph et al., 2015; Lau et al., 2016). One source of buoyancy is the thermal expansion of mantle material in proximity to the Earth's hot core. Other sources are also likely, including density differences associated with deep mantle structures that have been identified seismically by low shear wave velocities. An understanding of whether these structures are largely static or highly dynamic is critical for determining the mantle's ability to absorb core heat flow (Nakagawa and Tackley, 2014).

It is possible to construct an understanding of core heat flow and its connection to heat transport from the deep mantle from assumptions of the thickness of and temperature contrast across the thermal boundary layer (Tang et al., 2014; Stackhouse et al., 2015) but uncertainties are large (see, e.g., Figure 5 in Tang et al.,

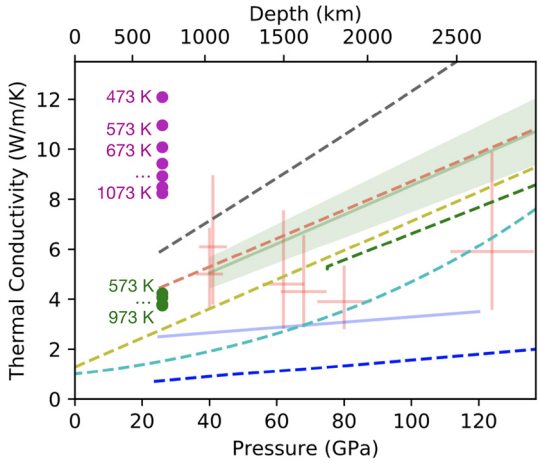

Fig. 5. Thermal conductivity of pyrolite and bridgmanite at 1900 to 2900 K, except where noted to be < 1900 K. Pyrolite is represented as in Fig. 4: red are our experimental data; green is from Stackhouse et al. (2015); and blue is from Tang et al. (2014). Bridgmanite experimental data at 470 to 1070 K of Manthilake et al. (2011) are shown by magenta circles ($MgSiO_3$ bridgmanite) and green circles ($Mg_{0.97}Fe_{0.03}SiO_3$ bridgmanite). Calculations interpolated to 2500 K for $MgSiO_3$ bridgmanite are shown as dashed lines: Haigis et al. (2012) in grey, Ammann et al. (2014) in orange; Ghaderi et al. (2017) in yellow; Stackhouse et al. (2015) in green; Dekura et al. (2013) in cyan; Tang et al. (2014) in blue.

2014). A simple calculation shows the inherent impact due to multiplication of these uncertainties. If we assume a range of core heat flow, $Q = 7$ to 15.5 TW, a range of thermal conductivity, $k = 3$ to 10 W/m/K, and a temperature jump across the thermal boundary layer, $\Delta T = 600$ to 2000 K, then we would determine a thermal boundary layer thickness, δ, that is between 32 and 360 km by using the equation

$$Q = \frac{k \Delta T A_{\mathrm{CMB}}}{\delta}$$

where $A_{\mathrm{CMB}} = 1.5 \times 10^{14}$ m^2 is the surface area of the core-mantle boundary. To arrive at a more precise prediction, we clearly need a significant reduction in the uncertainties of the governing parameters including the thermal conductivity.

It remains critically important to continue to improve our understanding about material properties of the deep Earth as the combination of high-pressure petrological studies, geodynamical model simulations, and quantitative comparisons with seismological observations and models (e.g., Ritsema et al., 2007; Jones et al., 2019) should eventually allow us to develop a deep understanding of the way the planet loses its internal heat.

Acknowledgements

We thank Suzy Vitale for performing the FIB milling, Emma Bullock for assistance with the SEM analysis, Nick Holtgrewe for computer codes to reduce streak camera data, and two anonymous referees for constructive reviews. This project was sponsored by a Carnegie Venture Postdoctoral Fellowship to ZMG. JB acknowledges support from IPGP multidisciplinary program PARI, Region Île-de-France SESAME Grant no. 12015908. AFG acknowledges support from NSF EAR 17632287.

Appendix A. Supplementary material

Supplementary material related to this article can be found online at https://doi.org/10.1016/j.epsl.2020.116161.

References

Alnæs, M.S., Blechta, J., Hake, J., Johansson, A., Kehlet, B., Logg, A., Richardson, C., Ring, J., Rognes, M.E., Wells, G.N., 2015. The FEniCS project version 1.5. Arch. Numer. Softw. 3, 9–23. https://doi.org/10.11588/ans.2015.100.20553.

Ammann, M.W., Walker, A.M., Stackhouse, S., Wookey, J., Forte, A.M., Brodholt, J.P., Dobson, D.P., 2014. Variation of thermal conductivity and heat flux at the Earth's core mantle boundary. Earth Planet. Sci. Lett. 390, 175–185. https://doi.org/10.1016/j.epsl.2014.01.009.

Brown, J.M., Shankland, T.J., 1981. Thermodynamic parameters in the Earth as determined from seismic profiles. Geophys. J. Int. 66, 579–596. https://doi.org/10.1111/j.1365-246X.1981.tb04891.x.

Chen, B., Gleason, A.E., Yan, J.Y., Koski, K.J., Clark, S., Jeanloz, R., 2010. Elasticity, strength, and refractive index of argon at high pressures. Phys. Rev. B 81, 144110. https://doi.org/10.1103/PhysRevB.81.144110.

Dalton, D.A., Hsieh, W.P., Hohensee, G.T., Cahill, D.G., Goncharov, A.F., 2013. Effect of mass disorder on the lattice thermal conductivity of MgO periclase under pressure. Sci. Rep. 3, 2400. https://doi.org/10.1038/srep02400.

Dekura, H., Tsuchiya, T., Tsuchiya, J., 2013. Ab initio lattice thermal conductivity of $MgSiO_3$ perovskite as found in Earth's lower mantle. Phys. Rev. Lett. 110, 025904. https://doi.org/10.1103/PhysRevLett.110.025904.

Ghaderi, N., Zhang, D.B., Zhang, H., Xian, J., Wentzcovitch, R.M., Sun, T., 2017. Lattice thermal conductivity of $MgSiO_3$ perovskite from first principles. Sci. Rep. 7, 5417. https://doi.org/10.1038/s41598-017-05523-6.

Goncharov, A.F., Beck, P., Struzhkin, V.V., Haugen, B.D., Jacobsen, S.D., 2009. Thermal conductivity of lower-mantle minerals. Phys. Earth Planet. Inter. 174, 24–32. https://doi.org/10.1016/j.pepi.2008.07.033.

Goncharov, A.F., Lobanov, S.S., Tan, X., Hohensee, G.T., Cahill, D.G., Lin, J.F., Thomas, S.M., Okuchi, T., Tomioka, N., 2015. Experimental study of thermal conductivity at high pressures: implications for the deep Earth's interior. Phys. Earth Planet. Inter. 247, 11–16. https://doi.org/10.1016/j.pepi.2015.02.004.

Haigis, V., Salanne, M., Jahn, S., 2012. Thermal conductivity of MgO, $MgSiO_3$ perovskite and post-perovskite in the Earth's deep mantle. Earth Planet. Sci. Lett. 355–356, 102–108. https://doi.org/10.1016/j.epsl.2012.09.002.

Hsieh, W.P., Deschamps, F., Okuchi, T., Lin, J.F., 2017. Reduced lattice thermal conductivity of Fe-bearing bridgmanite in Earth's deep mantle. J. Geophys. Res., Solid Earth 122, 4900–4917. https://doi.org/10.1002/2017JB014339.

Hsieh, W.P., Deschamps, F., Okuchi, T., Lin, J.F., 2018. Effects of iron on the lattice thermal conductivity of Earth's deep mantle and implications for mantle dynamics. Proc. Natl. Acad. Sci. 115, 4099–4104. https://doi.org/10.1073/pnas.1718557115.

Imada, S., Ohta, K., Yagi, T., Hirose, K., Yoshida, H., Nagahara, H., 2014. Measurements of lattice thermal conductivity of MgO to core-mantle boundary pressures. Geophys. Res. Lett. 41, 4542–4547. https://doi.org/10.1002/2014GL060423.

Jones, T.D., Maguire, R., van Keken, P., Ritsema, J., Koelemeijer, P., 2019. Subducted oceanic crust as the origin of seismically slow lower-mantle structures. https://doi.org/10.31223/osf.io/k98p7.

Katsura, T., Yoneda, A., Yamazaki, D., Yoshino, T., Ito, E., 2010. Adiabatic temperature profile in the mantle. Phys. Earth Planet. Inter. 183, 212–218. https://doi.org/10.1016/j.pepi.2010.07.001. Special Issue on Deep Slab and Mantle Dynamics.

Konôpková, Z., McWilliams, R.S., Gómez-Pérez, N., Goncharov, A.F., 2016. Direct measurement of thermal conductivity in solid iron at planetary core conditions. Nature 534, 99–101. https://doi.org/10.1038/nature18009.

Lau, H., Mitrovica, J., Austermann, J., Crawford, O., Al-Attar, D., Latychev, K., 2016. Inferences of mantle viscosity based on ice age data sets: radial structure. J. Geophys. Res., Solid Earth 121, 6991–7012. https://doi.org/10.1002/2016JB013043.

Lobanov, S., Holtgrewe, N., Ito, G., Badro, J., Piet, H., Nabiei, F., Lin, J., Bayarjargal, L., Wirth, R., Schriber, A., Goncharov, A., 2019a. Blocked radiative heat transport in the hot pyrolitic lower mantle. https://arxiv.org/pdf/1911.04136.pdf.

Lobanov, S., Holtgrewe, N., Lin, J.F., Goncharov, A., 2017. Radiative conductivity and abundance of post-perovskite in the lowermost mantle. Earth Planet. Sci. Lett. 479, 43–49. https://doi.org/10.1016/j.epsl.2017.09.016.

Lobanov, S., Soubiran, F., Holtgrewe, N., Badro, J., Lin, J., Goncharov, A., 2019b. Opaque lowermost mantle. https://arxiv.org/pdf/1909.01438.pdf.

Manthilake, G.M., de Koker, N., Frost, D.J., McCammon, C.A., 2011. Lattice thermal conductivity of lower mantle minerals and heat flux from Earth's core. Proc. Natl. Acad. Sci. 108, 17901–17904. https://doi.org/10.1073/pnas.1110594108.

McWilliams, R.S., Konôpková, Z., Goncharov, A.F., 2015. A flash heating method for measuring thermal conductivity at high pressure and temperature: application to Pt. Phys. Earth Planet. Inter. 247, 17–26. https://doi.org/10.1016/j.pepi.2015.06.002.

Mitrovica, J., Forte, A., 1997. Radial profile of mantle viscosity: results from the joint inversion of convection and postglacial rebound observables. J. Geophys. Res., Solid Earth 102, 2751–2769. https://doi.org/10.1029/96JB03175.

Nakagawa, T., Tackley, P., 2014. Influence of combined primordial layering and recycled MORB on the coupled thermal evolution of Earth's mantle and core. Geochem. Geophys. Geosyst. 15, 619–633. https://doi.org/10.1002/2013GC005128.

Ohta, K., Yagi, T., Taketoshi, N., Hirose, K., Komabayashi, T., Baba, T., Ohishi, Y., Hernlund, J., 2012. Lattice thermal conductivity of $MgSiO_3$ perovskite and

post-perovskite at the core–mantle boundary. Earth Planet. Sci. Lett. 349–350, 109–115. https://doi.org/10.1016/j.epsl.2012.06.043.

Okuda, Y., Ohta, K., Yagi, T., Sinmyo, R., Wakamatsu, T., Hirose, K., Ohishi, Y., 2017. The effect of iron and aluminum incorporation on lattice thermal conductivity of bridgmanite at the Earth's lower mantle. Earth Planet. Sci. Lett. 474, 25–31. https://doi.org/10.1016/j.epsl.2017.06.022.

Pozzo, M., Davies, C., Gubbins, D., Alfè, D., 2012. Thermal and electrical conductivity of iron at Earth's core conditions. Nature 485, 355–358. https://doi.org/10.1038/nature11031.

Rainey, E.S.G., Kavner, A., 2014. Peak scaling method to measure temperatures in the laser-heated diamond anvil cell and application to the thermal conductivity of MgO. J. Geophys. Res., Solid Earth 119, 8154–8170. https://doi.org/10.1002/2014JB011267.

Ritsema, J., McNamara, A., Bull, A., 2007. Tomographic filtering of geodynamic models: implications for model interpretation and large-scale mantle structure. J. Geophys. Res., Solid Earth 112, B01303. https://doi.org/10.1029/2006JB004566.

Rudolph, M., Lekic, V., Lithgow-Bertelloni, C., 2015. Viscosity jump in Earth's mid-mantle. Science 350, 1349–1352. https://doi.org/10.1126/science.aad1929.

Stackhouse, S., Stixrude, L., Karki, B.B., 2015. First-principles calculations of the lattice thermal conductivity of the lower mantle. Earth Planet. Sci. Lett. 427, 11–17. https://doi.org/10.1016/j.epsl.2015.06.050.

Tang, X., Ntam, M.C., Dong, J., Rainey, E.S.G., Kavner, A., 2014. The thermal conductivity of Earth's lower mantle. Geophys. Res. Lett. 41, 2746–2752. https://doi.org/10.1002/2014GL059385.